ORIGINAL ARTICLE

Specified iron oxide nanoparticles by PSMA-11 as a promising nanomolecular imaging probe for early detection of prostate cancer

Farzaneh Ghorbani[1,2] · Rasoul Irajirad[3] · Farshad Emami[4] · Fereshteh Vaziri Nezamdoust[1] · Alireza Montazerabadi[1]

Abstract

PSMA-11-HBED and PSMA-11-HYNIC are well-known prostate cancer (PCa) ligands, which strongly bind to prostate-specific membrane antigen (PSMA) on PCa epithelial cells. In this study, we announced the synthesis, physico-chemical properties and in vitro binding assay of targeted iron oxide nanoparticles (IONPs) by the PSMA-11 peptides as an MRI nanocontrast agent for early PCa discernment. IONPs were coated with carboxymethylated dextran (CMD-IONPs) and also with bovine serum albumin (BSA-IONPs), then conjugated with two different amounts of PSMA-11-HYNIC (T-CMD-IONPs) and PSMA-11-HBED (T-BSA-IONPs). In addition, the cellular viability, relaxometry measurements in aqueous and in vitro media, as well as quantitative cell uptake of the synthesized formulations were evaluated. At diagnostic concentrations, IONPs showed no cytotoxicity. A comparison of T-BSA-IONPs and T-CMD-IONPs with non-targeted IONPs at concentration $750\,\mu M$ indicates that LNCaP PSMA + prostate cancer cells took up, respectively, 5.02 and 1.77 times as much IONPs. The results validated distinguished $r_2 (mM^{-1}s^{-1})$ values at $1.5\,T$ MRI scanner as 160 for CMD-IONPs and 68 for BSA-IONPs. Moreover, targeted-IONPs *in-vitro* had higher r_2 values than untargeted IONPs. The contrast to noise ratio (CNR) between targeted and non-targeted IONPs at concentration $750\,\mu M$ were calculated as 4.65 and 3.95 for T-BSA-IONPs and T-CMD-IONPs, respectively. The study confirms that the novel T-BSA-IONPs and T-CMD-IONPs nanoprobes are suitable negative contrast agents for molecular imaging of PCa.

Keywords Iron oxide nanoparticles (IONPs) · PSMA · PSMA-11 · Targeted imaging · Molecular imaging · Prostate cancer · Magnetic resonance imaging

✉ Alireza Montazerabadi
alireza.montazerabadi@gmail.com

Farzaneh Ghorbani
ghorbanifme@gmail.com

[1] Medical Physics Research Center, Mashhad University of Medical Sciences, Mashhad, Iran

[2] Student Research Committee, Mashhad University of Medical Sciences, Mashhad, Iran

[3] Finetech in Medicine Research Center, Iran University of Medical Sciences, Tehran, Iran

[4] Cancer Research Center, RAZAVI Hospital, Imam Reza International University, Mashhad, Iran

Introduction

Prostate cancer (PCa) is the most prevalent and second leading cause of death among men (Patel et al. 2019). An accurate and specific diagnostic method leads to early cognizance of patients, hence improving their prognosis (Catalona et al. 1994). Currently, transrectal ultrasonography-guided biopsy (TRUS) is applied as a definitive method for men with elevated levels of prostate-specific antigen (PSA) in their blood and who are also suspected of having PCa based on a digital rectal examination (DRE). But forasmuch as the samples are randomly selected, the sensitivity of TRUS is less than 50%. Table 1 shows that none of these diagnostic approaches combine high sensitivity and specificity at the same time, so they cannot be used exclusively for diagnosing and treating PCa (Patel et al. 2019; Guthman et al. 1993; Basha et al. 2019; Sun et al. 2016). The methods with the most specificity are biopsy, as a gold standard, and PET/CT, which uses a specific PCa ligand. Obtaining biopsy

specimens randomly makes this method insensitive. MRI, moreover, has the potential to be the most sensitive method for diagnosing PCa.

Besides, among medical imaging methods, MRI is an extremely useful modality because it offers excellent soft tissue contrast, imaging in various anatomical directions, non-ionizing radiation, and the possibility of using contrast media (Sun et al. 2016; Abd Elrahman and Mansour 2019). To this end, many studies have been conducted to develop targeted agents for MRI sequences which significantly increase the specificity of this method.

In this regard, most studies have been performed using the J591 antibody as a specific PCa ligand (Abdolahi et al. 2013; Taylor et al. 2011; Bates et al. 2014; Abraham et al. 2017). However, the use of antibodies has some limitations such as low tumor permeability, long delay between injection and imaging, non-specific accumulation associated with inflammation, and prolonged plasma presence (Rahbar et al. 2018). Therefore, there is a growing interest in using peptides and small molecule inhibitors as specific ligands.

In this framework, iron oxide nanoparticles (IONPs) can be used as contrast agents to enhance MRI capabilities for accurate diagnosis (Abd Elrahman and Mansour 2019; Ngen et al. 2019; Nagesh et al. 2016; Yu et al. 2011; Montazerabadi et al. 2015). So far, IONPs have been introduced for a wide range of diagnostic and therapeutic applications, such as hyperthermia and photothermal remedies, drug release and molecular imaging, which are still being developed (Ghorbani et al. 2018; Li et al. 2013).

The manipulation of targeted IONPs with specific PCa ligands such as antibodies, peptides, and aptamers, can dramatically increase their specificity (Abdolahi et al. 2013; Taylor et al. 2011; Bates et al. 2014; Abraham et al. 2017; Abd Elrahman and Mansour 2019; Ngen et al. 2019; Nagesh et al. 2016; Yu et al. 2011; Frtús et al. 2020).

Furthermore, prostate-specific membrane antigen (PSMA) is a type II membrane protein with folate hydrolase activity, which is produced by the prostatic epithelium (Ahn et al. 2019). There is a direct correlation between its expression level and malignancy degree, while 94% of primary prostate cancers exhibit PSMA expression. Also, small molecule PSMA inhibitors can penetrate cells after binding to PSMA, which can lead to improvements in imaging and therapy. In this way, using a contrast agent which targets PSMA will provide a targeted diagnosis method (Kiess et al. 2015). PSMA-11 is a PCa-specific ligand that strongly binds to the extracellular moiety of PSMA (Afshar-Oromieh et al. 2016). It is already being used clinically as:

- $PSMA - 11 - HBED -^{68}Ga$ at PET/CT, (Rahbar et al. 2018)
- $PSMA - 11 - HYNIC -^{99}Tc$ at SPECT/CT. (Silong et al. 2016)

Here, we tailored IONPs that were coated with both bovine serum albumin (BSA-IONPs) and carboxymethylated dextran (CMD-IONPs) to enhance their stability and biocompatibility and subsequently provide a surface for binding PSMA-11 as well. Chemical bonds were established for PSMA-11-HBED on BSA-IONPs and PSMA-11-HYNIC on CMD-IONPs. The physical and chemical properties as well as the provided contrast by these two specified IONPs on PSMA + LNCaP prostate cancer cell line were evaluated. Fig.1 shows a schematic representation of the study.

Methods

Synthesis of specified IONPs

The coated IONPs were synthesized using a co-precipitation method. Next the PSMA-11 ligand was covalently linked to the coated IONPs at two different concentrations.

CMD-IONPs–PSMA-11

The details of IONPs coated with carboxymethylated dextran (CMD) (IONPs-CMD), were published in our previous study (Yousefvand et al. 2021). Briefly, in the first step, dextran (Sigma; average MW: $9 - 11\,kDa$, CAS No: 9004-54-0) was carboxymethylated and then $1\,g$ CMD was dissolved in $25\,mL$ deionized water. In the second step, iron (II) chloride tetrahydrate ($FeCl_2.4H_2O$, Merck, CAS No: 13478-10-9) and iron (III) chloride hexahydrate ($FeCl_3.6H_2O$, Merck, CAS No: 10025-77-1) in the molar ratio 2:1 were added to CMD and was stirred for 15 min. Next, $5\,mL$ of 25% ammonium hydroxide (NH_4OH, Merck, CAS No: 1336-21-6) was added slowly to this solution until the pH reaches 12, while stirring under N_2 atmosphere at 10 °C. Then, the suspension was heated up to 78 °C for 1 h.

In the third step, the amine group of PSMA-11-HYNIC (Kimia Pajouh Dorsa Co., Iran) was covalently linked to carboxyl-modified IONPs-CMD. This step is the same as our previous study on triptorelin peptide (Yousefvand et al. 2021). In this step, the targeted CMD-IONPs (T-CMD-IONPs) were prepared with two different amounts of PSMA-11-HYNIC as $C_1 = (3\,mg/L$ IONPs : $0.1\,mg$ peptide) and $C_2 = (3\,mg/L$ IONPs : $0.5\,mg$ peptide). The T-CMD-IONPs were set to neutral pH and dialyzed by a membrane bag with a 12, 000 cutoff molecular weight for 24 h to emit the non-attached PSMA-11-HYNIC and also the very low probable amount of non-reacted cyanogen bromide (BrCN, Sigma, C91492) in the solution.
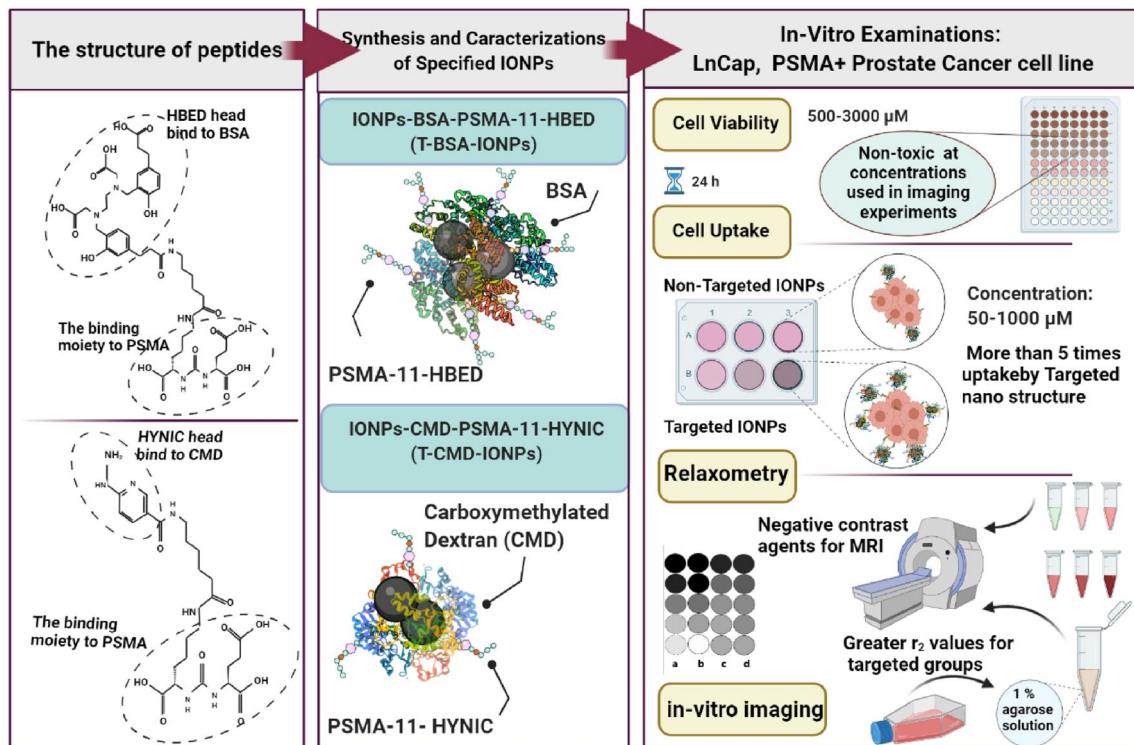
Fig. 1 Schematic illustration of chemical structures of PSMA-11-HBED and PSMA-11-HYNIC, the synthesized targeted IONPs and an overview of in-vitro examinations.

BSA-IONPs-PSMA-11

IONPs coated with bovine serum albumin (BSA, Merck, Germany; MW: 69 kDa, CAS No: 9048-46-8) (IONPs-BSA) were synthesized using a co-precipitation method (Nosrati et al. 2018). In the first step, 40 mL deionized water was under N_2 atmosphere for 30 min. 1.5 g BSA was dissolved in the water and the temperature was raised to 48 °C. Next, 200 mg $FeCl_2.4H_2O$ and 550 mg $FeCl_3.6H_2O$ in the molar ratio 2:1 were added to BSA and stirred for 15 min. Then, 5 mL of 25% ammonium hydroxide (NH_4OH) was added drop by drop to this solution. The reaction was continued for 2 h at 48 °C. Due to the specificity of BSA in pH regulation, BSA-IONPs are pH neutral at the end of synthesis.

The component was then dialyzed at 4°C for 24 h to remove ammonia salts. The targeted BSA-IONPs (T-BSA-IONPs) were prepared with two different amounts of PSMA-11-HBED (Kimia Pajouh Dorsa Co., Iran, CAS No: 1366302-52-4) as $C_1 = (3 \, mg/L$ IONPs : 0.1 mg peptide) and $C_2 = (3 \, mg/L$ IONPs : 0.5 mg peptide).

In the second step, the carboxyl groups of PSMA-11-HBED were linked covalently to the amine groups on BSA. To this approach, 0.5 mg N-(3-Dimethylaminopropyl)-N'-ethylcarbodiimide hydrochloride (EDC, Merck, CAS No: 25952-53-8) was stirred with PSMA-11-HBED for 30 min. Next, 3 mg/L BSA-IONPs was added slowly to the solution.

The reaction was continued at 4 °C for 24 h. The targeted BSA-IONPs (T-BSA-IONPs) were set to neutral pH and dialyzed by a membrane bag with a 12,000 cutoff molecular weight for 24 h to emit non-attached PSMA-11-HBED and also a very low probable amount of EDC in the solution.

Physico-chemical characterizations

Hydrodynamic diameter, size distribution and zeta potential of the targeted (T-BSA-IONPs, T-CMD-IONPs) and non-targeted (BSA-IONPs, CMD-IONPs) nanostructures were measured by a dynamic light scattering (DLS) instrument with the detection angle of 90 at 25 °C (Zetasizer, Malvern Ins., USA). The UV–Vis (UV 1700, Shimadzu Corp., Japan) absorption spectra of the mentioned IONPs were used to find the absorption rate changes due to benzene group in PSMA-11. The morphology of IONPs-CMD and IONPS-BSA was observed by transmission electron microscopy (TEM; Philips CM120, Philips Electron Optics, Netherland). The crystal lattice properties were indicated by powder X-ray diffraction (XRD; GNR EXPLORER, Italy) with 2θ range of 20–80 at wavelength $\lambda = 1.5418$ Å. The functional groups and chemical structural changes in targeted and non-targeted IONPs were ascertained using Fourier-transform infrared spectroscopy (FTIR; Spectrum two, PerkinElmer, USA). A vibrating sample magnetometer (VSM; Danesh Pajoush

Magnetis Company of Kashan, VSMF model, Iran) was used to evaluate the magnetic field-dependent magnetization under circulate magnetic field in the range of -14000 up to $14000\ Oe$ at 27 °C. Thermogravimetric analysis (TGA; PerkinElmer, Waltham, MA) of BSA-IONPs and CMD-IONPs was obtained to appraise the mass of coated BSA and CMD on IONPs surfaces.

In vitro examinations

Lymph node carcinoma of prostate (LNCaP) cell line (National Cell Bank of Iran, Pasteur Institute of Iran) was cultured in DMEM high glucose with 10% of fetal bovine serum (FBS; Gibco, UK) at 37 °C under 5% CO_2 in a moist incubator. The medium was supplemented with penicillin ($100\ U/mL$) and streptomycin ($100\ \mu g/mL$) (Pan Biotech, Aidenbach, Germany). The cells were counted using trypan blue (Sigma, USA) method.

Cell viability assay

Cells were seeded at a density of 12×10^3 per well in a 96-well culture plate and incubated overnight at 37 °C C in air containing 5% CO_2. Different concentrations of targeted and non-targeted IONPs (C_2; $500 - 3000\ \mu M$) were separately applied to cells. After 24h , the medium was removed and cells were washed three times with PBS. Finally, the MTT assay was performed.

In this regard, $100\ \mu L$ culture medium-free FBS and $10\ \mu L$ MTT (2,5-diphenyltetrazolium bromide, Sigma Aldrich, Germany) were added to each well. 4 h incubation at 37 °C in darkness led to the formation of formazan dye. The medium was removed and $200\ mL/well$ dimethyl sulfoxide (DMSO, Sigma Aldrich, Germany) was added for cell lysis. The plate was shaken for 10 min to dissolve the formazan product. An ELISA reader (Stat Fax-2100 Awareness, USA) was used to read the absorbance at wavelengths of $540\ nm$ and $630\ nm$. The cell survival (S%) at concentration x was calculated using Eq. 1 as follows:

$$S_x(\%) = \frac{(A_{IONPs})_x - (B_{IONPs})_x}{A_{control} - B_{control}} \times 100, \tag{1}$$

where A_{IONPs} and $A_{control}$ are the absorbance of the treated group with IONPs and the control group, respectively. B_{IONPs} and $B_{control}$ are related to the absorbance of the cell media with and without IONPs as blank. The experiment was repeated three times.

Cellular uptake

The LNCaP cancer cells were seeded in six-well plates at a density of 5×10^5 cells/well and incubated overnight. After

24 h incubation with various concentrations of targeted and non-targeted IONPs (C_1 and C_2; $50 - 1000\ \mu M$), cells were washed three times with PBS and $0.4\ mL$ Trypsin–EDTA (Sigma, USA) was added to each well. The content of each well was transferred to an $1.5\ mL$ microtube and centrifuged at $3,000$ rpm for $5\ min$. The supernatant was slowly drained and cells were broken down with perchloric acid ($HClO^4$, Merck, Germany). Subsequently, the amount of Fe in each sample was estimated with atomic absorption spectroscopy (AAS).

MRI examinations

Relaxometry

As a result of the presence of contrast agents, the signal intensity changes with the longitudinal and transverse relaxation times (T_1 and T_2) of protons within each voxel. The relaxation rates (R_1 and R_2) indicate the T_1 and T_2 changes based on a linear function of concentration (Sillerud 2016) as follows:

$$R_{1,2} = \frac{1}{T_{1,2}} = \frac{1}{T_{1,2}^0} + r_{1,2} \times C, \tag{2}$$

where:

- C is the concentration of the contrast agent,
- r_1 and r_2 are related to the contrast agent,
- T_1^0 and T_2^0 are related to deionized water,
- T_1 and T_2 are related to aqueous medium containing the contrast agent.

The r_1 and r_2 of synthesized IONPs were measured by imaging various concentrations (C_1; 750, 500, 250, 125, 62.5 and $31.2\ \mu M$) at 1.5 Tesla MRI scanner (Philips, Qaem Hospital). T_1-weighted spin echo images were acquired at TE:$24\ ms$; TR_1 to TR_6: 100, 300, 600, 900, 1500 ms; flip angle: 90 degree; matrix size: 256×256; field of view (FoV): $200\ mm$, 100%; echo train length: 1; slice thickness: $3\ mm$. As TR was decreased, the number of averages was increased to maintain the signal to noise ratio (SNR) at 1.01.

T_2-weighted images were obtained via a T_2 multi-spin echo pulse sequence by fixed TR at 2000 ms; TE_1 to TE_{16}: $20 : 20 : 320\ ms$; flip angle: 180 degree; matrix size: 256×256; FoV: $200\ mm$, 100%; averages: 1, echo train length: 1. All curve fitting routines, which were used to determine the relaxation rates, were performed by RadiAnt Dicom riewer and Origin Softwares. The r_2 and r_1 values were attained by plotting signal intensities versus different TEs and TRs, respectively. Afterward, the $1/T_2$ (and $1/T_1$) was acquired by fitting the following Equation 3 and (Equation 4) on the data at each concentration:

$$SI = S_0. \exp(-t/T_2), \tag{3}$$

$$SI = S_0.(1 - \exp(-t/T_1)). \tag{4}$$

Thereafter, regarding Eq. (2), the relaxation rate r_2 (and r_1) was estimated as the slope of the fitted linear curve on $1/T_2$ (and $1/T_1$) versus concentration.

Magnetic resonance imaging

The accumulation of targeted and non-targeted IONPs within LNCaP cells was embodied using MRI modality. The cells were seeded in T25 flasks at a density of 2×10^6 and incubated overnight. Four concentrations (C_1; 1500, 750, 375 and 187 μM) of every four synthesized IONPs were separately added to each T25 flask and incubated for 24 h. Then, cells were washed three times with PBS, and 1.5 mL Trypsin–EDTA was added to each flask. The content of each flask was transferred to a 2 mL microtube and centrifuged at 3,000 rpm for 5 min. The supernatant was slowly drained and agarose solution (1%) was added to cells. Cells in agarose without incubation with IONPs were used as the control group. The acquisition parameters were selected the same as that of the relaxometry examination.

Statistical analysis

SPSS 24 was used for data analysis. The non-parametric Kolmogorov–Smirnov test was used to assess the normality of data. One-way ANOVA followed by Tukey's multiple comparison tests were used to analyze statistical differences ($P < 0.05$).

Results

Size, morphology and stability

Figure 2 illustrates the zeta potential and also the particle size of the synthesized IONPs in deionized water after 1 h and 4 h incubation in DMEM high glucose cell medium with 10% FBS. There was no significant difference between nanoparticles in deionized water and cell culture medium. This corroborates the stability of IONPs in biological environments. The zeta potential for BSA-IONPs, T-BSA-IONPs, CMD-IONPs and T-CMD-IONPs was determined as -40, -26, -30 and -27 mV, respectively, which validates the stability of IONPs. TEM images were achieved 1 month post-synthesis, while IONPs were stored in PBS, pH 7.4 at 4 °C. The *spherical* and *homogeneous* morphology of IONPs are attested in Fig. 2. The attained size distribution histograms from TEM images using ImageJ software,

Fig. 2, exhibited an average size of 22.6 ± 4.5 nm (based on 60 nano-particles) for BSA-IONPs and 8.6 ± 1.6 nm (based on 52 nanoparticles) for CMD-IONPs.

Formation of IONPs

Figure 3 depict XRD diagrams of IONPs. The maximum peaks at 2θ values of 35.6° and 35.9°, respectively, for BSA-IONPs and CMD-IONPs, represent a typical Fe_3O_4 structure. The XRD spectra are consonant with the main peaks of standard magnetite Fe_3O_4, vertical dashed lines, according to JCPDS file, No. 19-0629 (Byong and Kwak 2010).

The weight ratios of IONPs in BSA-IONPs and CMD-IONPs were, respectively, estimated as 38% and 32% based on the weight loss profiles by the TGA analyzer.

Super-paramagnetic behavior

The VSM results confirmed the super-paramagnetic characteristic of BSA-IONPs and CMD-IONPs, which is very beneficial for subsequent nano-biomedical usages, Fig. 3. The saturation magnetization was achieved as 36 and 50 emu/g for BSA-IONPs and CMD-IONPs, respectively.

Evaluation of PSMA-11 binding on IONPs

In view of the fact that aromatic structures are capable of absorbing the UV photons, and considering the presence of the benzene group in the peptide structure, UV–Vis spectra of the synthesized IONPs were obtained. For both targeted formulations, forked absorption peaks are attained in the UV region (Topală et al. 2014; Jalali et al. 2014). Given that the absorption in the visible domain was exactly the same for the targeted and non-target nanoparticles, only the absorption at the UV region has been illustrated, Fig. 4. To clearly learn the structures of PSMA-11 peptides on the coated IONPs, FTIR spectra of the targeted and non-targeted IONPs were determined and compared together, Fig. 4. In the spectrum of BSA-IONPs, the peaks at 3143 cm^{-1}, 3039 cm^{-1}, 1655 cm^{-1}, and 620 cm^{-1} are, respectively, related to the primary amines and O–H bond, the C–H stretches, amide I and the Fe–O bond. The considerable peaks assigned to the structure of dextran are 3394 cm^{-1} (O–H), 2923 cm^{-1} (–CH2), 1557 cm^{-1} (carbonyl of aldehyde group) and 1011 cm^{-1} (C–O) (Doustkhah et al. 2019; Mikhaylova et al. 2004). As one can see in the CMD spectrum, the related absorption bond to carbonyl of aldehyde group is omitted as a result of dextran reduction and consequently the carbonyl bond of the asymmetric carboxyl group (1603 cm^{-1}) is formed because dextran is bonded to the organic acid. By complexation of the carbonyl group with the surface of IONPs, the 1603 cm^{-1} peak

Fig. 2 **a** The particle size distribution of the synthesized IONPs were measured in aqueous medium as well as in DMEM HG (10% FBS) for 1 h and 4 h, to test their stability. **c** Histogram of BSA-IONPs diameter based on 60 nanoparticles suggests $22.6 \pm 4.5 nm$. **e** Histogram of CMD-IONPs diameter based on 52 nanoparticles suggests $8.6 \pm 1.6 nm$
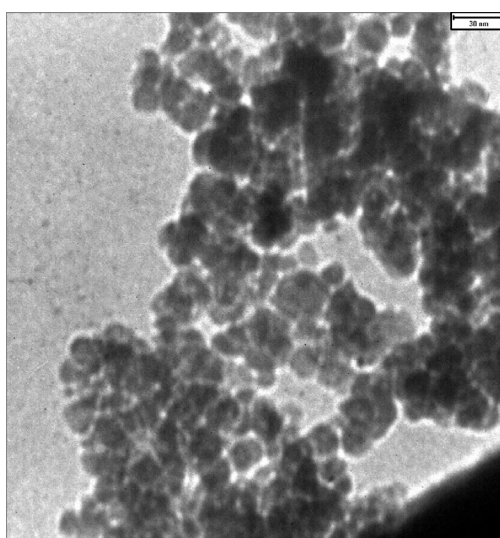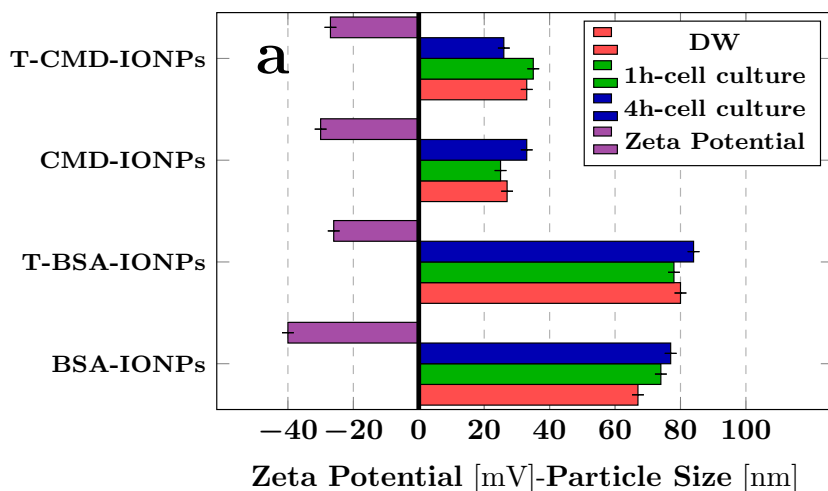
(b) TEM image of BSA-IONPs, $scale = 30\,nm$
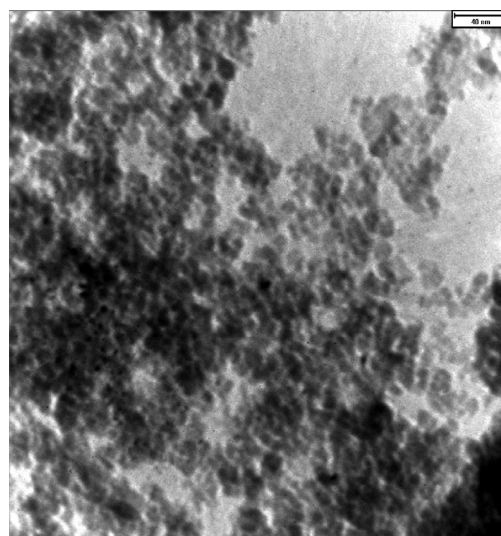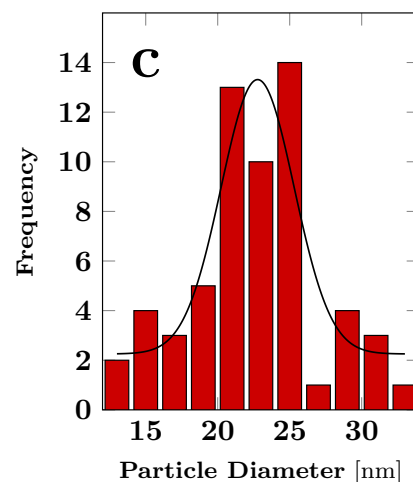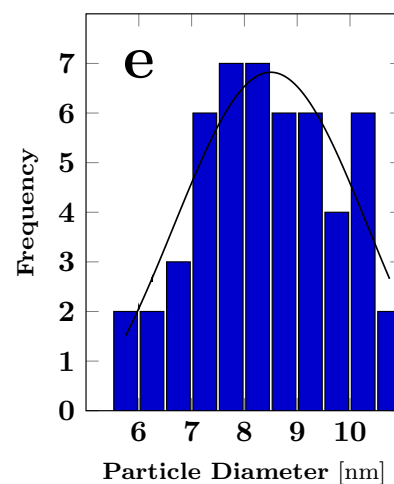

(d) TEM image of CMD-IONPs, $scale = 40\,nm$

Fig. 3 XRD pattern of **a** BSA-IONPs and **b** CMD-IONPs. The main peaks of standard magnetite Fe_3O_4 have been shown by vertical dashed lines. The XRD system acted at 40 kV and 30 mA in a 2θ range of 20–80 °C at $\lambda = 1.5418$ Å. **c** Magnetic hysteresis curve at the magnetic field in the range of 0 to 14 kOe at 27 °C. CMD-IONPs have a higher saturation magnetization than BSA-IONPs. **d** The weight loss profiles were obtained from 40–1000 °C at 10 °C/min. The results showed that BSA-IONPs and CMD-IONPs were, respectively, 38% and 32% naked IONPs
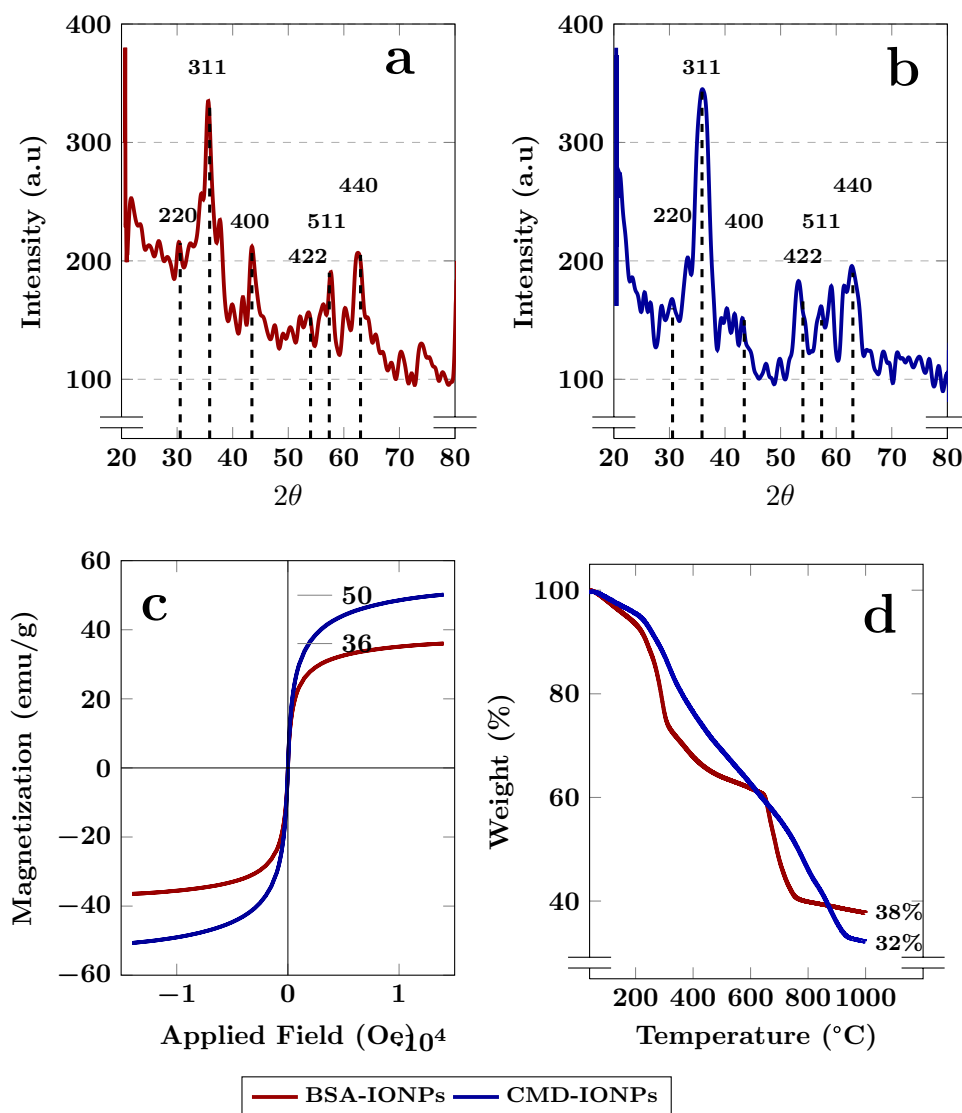
subsequently had a blue shift to 1583 cm^{-1} in the CMD-IONPs spectrum. Besides, the peak at 530 cm^{-1} is related to the Fe–O bonds of IONPs.

The targeted CMD-IONPs peak at 1637 cm^{-1}, which can be attributed to the presence of carbonyl groups in the peptide structure and an evidence that it binds to the surface of IONPs (Yousefvand et al. 2021). Therefore, the FTIR spectra results confirmed the surface modification of IONPs by PSMA-11 peptides.

The toxicity of the synthesized IONPs

The MTT results showed that cell viability, based on Eq. 1, at concentration 3 mM decreased up to 8.5 ± 0.3% for T-BSA-IONPs and up to 29.8 ± 2.2% for T-CMD-IONPs in comparison to untreated cells, Fig. 5. There

were significant differences between BSA-IONPs (at 3 mM), T-BSA-IONPs (for $\geq 1.5\,mM$), CMD-IONPs (for $\geq 1\,mM$) and T-CMD-IONPs (for $\geq 0.75\,mM$) with the control group.

Cellular uptake

Atomic absorption spectroscopy (AAS) results confirmed that the cellular uptake efficiency of targeted IONPs was better than that of non-targeted IONPs, Fig. 5 and Fig. 5. The cellular uptake increases with concentration (both C_1 and C_2), except for T-BSA-IONPs at (C_1 and C_2; 1000 μM). For T-BSA-IONPs, the maximum uptake occurred at 21 $pg/cell$ at (C_1; 750 μM) and 70 $pg/cell$ at (C_2; 750 μM). The uptake swiftly exceeded after (C_2; 500 μM) for T-BSA-IONPs. For T-CMD-IONPs, the maximum uptake occurred at 20 $pg/cell$ at (C_1; 1000 μM) and 32 $pg/cell$ at (C_2; 1000 μM). To get a better comparison, we defined the uptake Ratio (UR) as:

Fig. 4 The UV spectra at 150 μM of **a** BSA-IONPs and **b** CMD-IONPs. The FTIR spectra of **c** BSA-IONPs, T-BSA-IONPs and **d** carboxymethylated dextran (CMD), CMD-IONPs and T-CMD-IONPs.
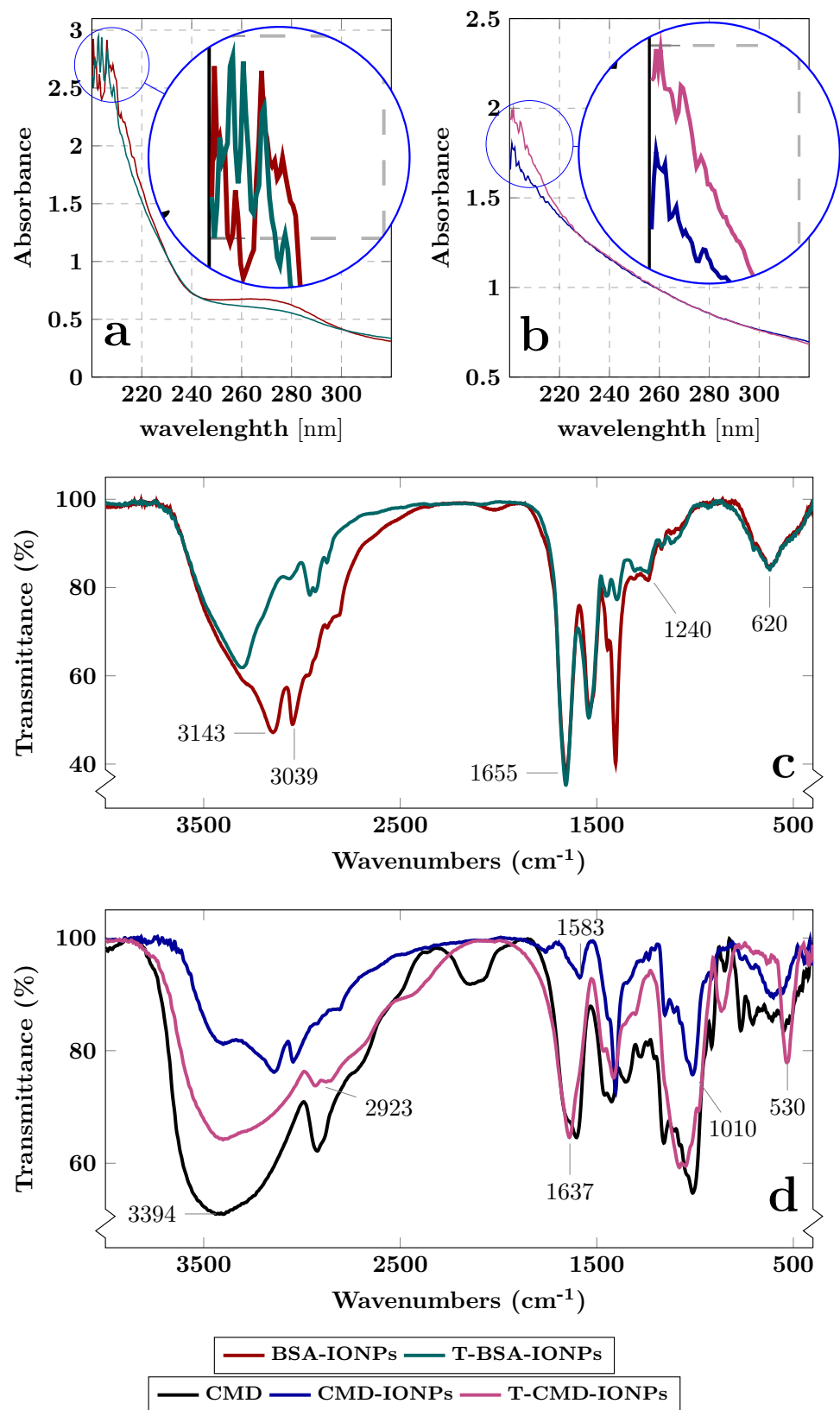
Fig. 5 The LNCaP cancer cells were seeded in 98-well plates (12×10^3 cells/well) for MTT assay and in six-well plates (5×10^5 cells/well) for the cell uptake test, then incubated 24 h with various concentrations of IONPs. **a** In vitro cytotoxicity. The cellular uptake by atomic absorption spectroscopy, at different ratios of IONPs to PSMA-11 **b** C_1 which is defined as $3\,mg/L$ of IONPs to $0.1\,mg$ PSMA-11. **c** C_2 which is defined as $3\,mg/L$ of IONPs to $0.5\,mg$ PSMA-11. Data are shown as $mean \pm SD\,(n = 3)$
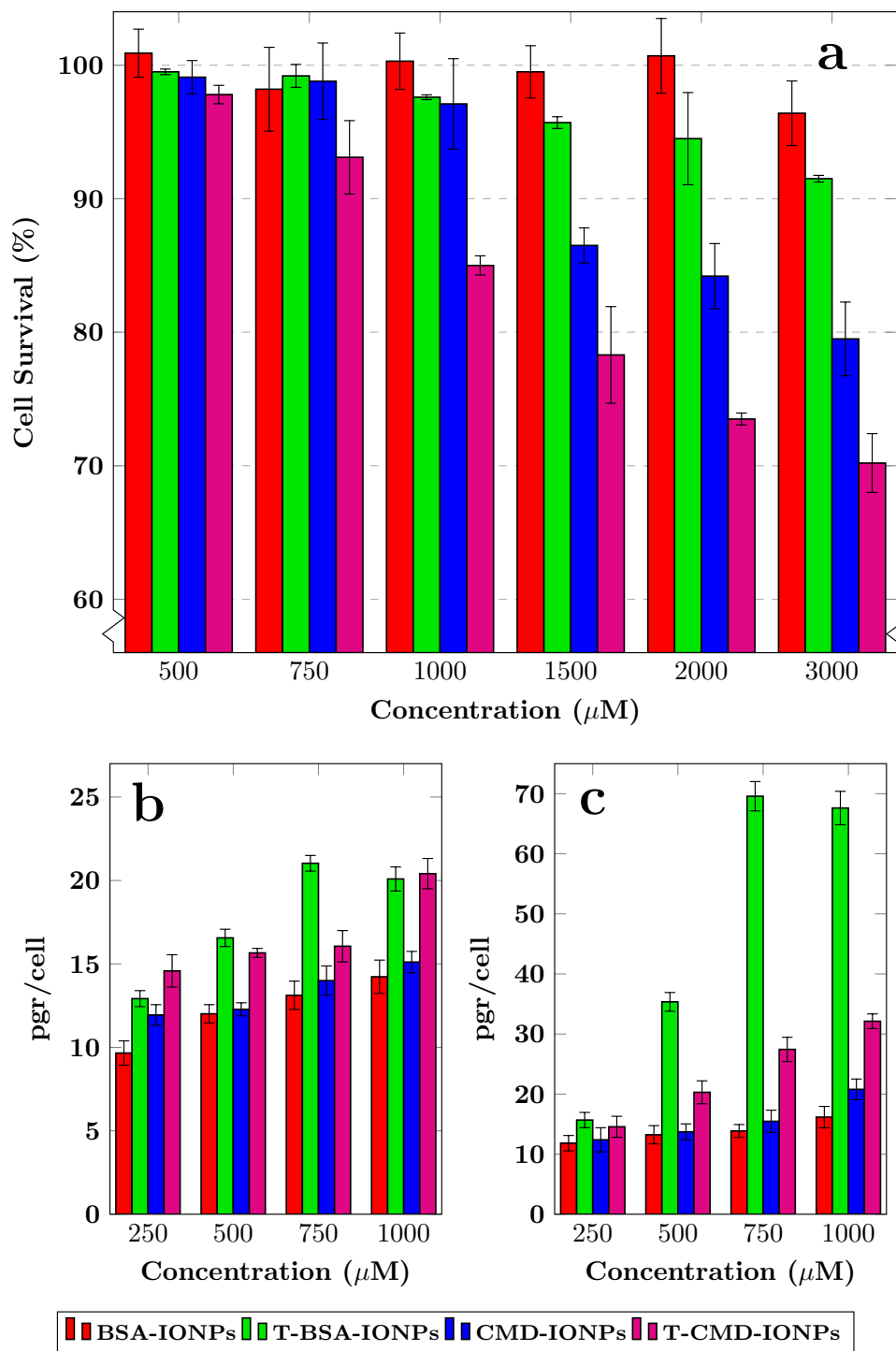
$$UR = \frac{uptake\ of\ targeted\ IONPs}{uptake\ of\ non\ targeted\ IONPs}. \qquad (5)$$

The UR values for each specified-IONPs at various concentrations are shown in Table 2. At all concentrations, the UR values were greater for BSA-IONPs than CMD-IONPs.

The uttermost URs were perceived for BSA-IONPs at (C_1 and C_2; $750\,\mu M$) and for CMD-IONPs at (C_1; $1000\,\mu M$) and (C_2; $750\,\mu M$).

Fig. 6 The MR images of targeted and non-targeted IONPs at 750 μM in (**a**, **e**) Deionized water and **c**, **g** 1% agarose phantom gels and their related signal intensity curves. T_1-W spin echo images (**e**, **g**) were acquired at TE: 24 ms; TR_1 to TR_6: 100, 300, 600, 900, 1500 ms. T_2-W images (**a**, **c**) were obtained with a T_2 multi-spin echo pulse sequence by fixed TR of 2000 ms; TE_1 to TE_{16}: 20 : 20 : 320 ms
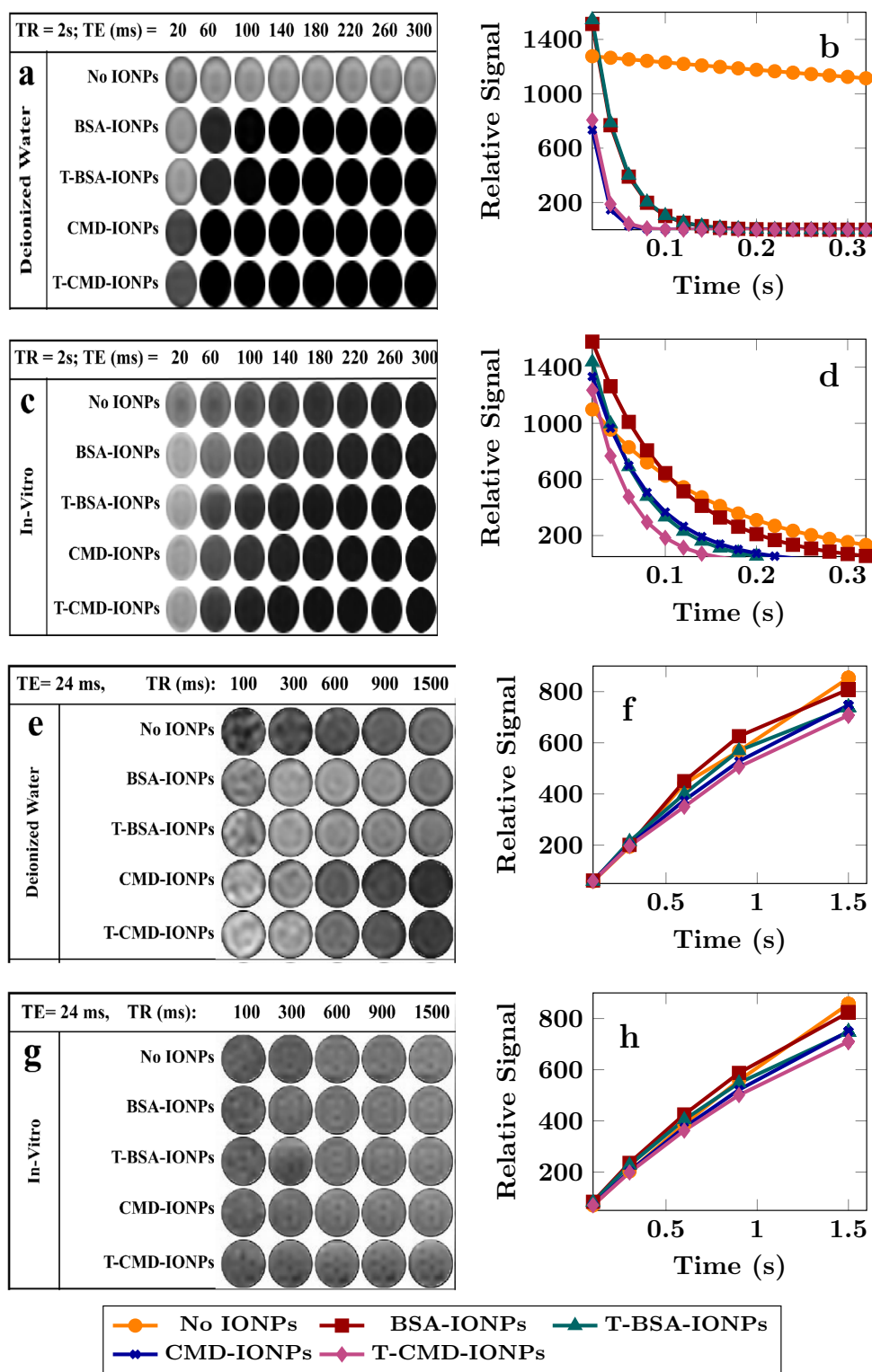
Magnetic resonance imaging

The MR images of IONPs at 750 μM in water and in in vitro media can be seen in Fig. 6. The r_1, r_2 and their ratio for targeted to non-targeted IONPs in deionized water and in in vitro situation are shown in Table 3. The greatest amounts of r_1 and r_2 in deionized water were obtained for CMD-IONPs, T-CMD-IONPs, and evenly for BSA-IONPs and T-BSA-IONPs. However, the r_2/r_1 ratio was maximum, respectively, for T-BSA-IONPs, BSA-IONPs,

Table 1 The most routine diagnostic methods of PCa

Diagnostic test	Specificity	Sensitivity
PSA level	85%	75%
DRE	40%	81%
TRUS	99%	48%
MRI	45%	93%
PET–CT	99%	77%

PSA Prostate-specific antigen, *DRE* Digital Rectal Examination, *TRUS* Transrectal ultrasound-guided biopsy

Table 2 The uptake ratio (UR) is defined as the ratio of Fe amount by AAS results in targeted to non-targeted group at the same concentration.

Concentration	BSA-IONPs		CMD-IONPs	
	C_1[a]	C_2[b]	C_1	C_2
250 μM	1.34	1.33	1.22	1.18
500 μM	1.38	2.67	1.28	1.48
750 μM	1.60	5.02	1.15	1.77
1000 μM	1.40	4.18	1.35	1.55

[a] C_1 = (3 mg/L IONPs : 0.1 mg peptide)

[b] C_2 = (3 mg/L IONPs : 0.5 mg peptide)

T-CMD-IONPs and CMD-IONPs. The utmost r_2 in *in-vitro* was sequentially ascertained for T-CMD-IONPs, T-BSA-IONPs, CMD-IONPs and BSA-IONPs. The r_1 has the same value for all targeted and non-targeted IONPs in in vitro. To consider the changes of r_1 and r_2 in water and in in vitro medium for targeted and non-targeted IONPs, we defined relaxation rate coefficient (RRC) as:

$$RRC_{1,2} = \left(\frac{r_{1,2-cell}}{r_{1,2-water}} \right)_T / \left(\frac{r_{1,2-cell}}{r_{1,2-water}} \right)_{NT}, \tag{6}$$

where:

- *T* is associated with targeted IONPs,
- *NT* is associated with non-targeted IONPs,
- *Cell* is related to the in vitro values,
- *Eater* is related to the *deionized water* values.

Table 4 The contrast to noise ratio (CNR) values between targeted and non-targeted IONPs, as well as between them and the control group (non-treated cells with IONPS) at 750 μM

Nanoprobe	T[a]-Cell	NT[b]-Cell[c]	T-NT
BSA-IONPs	7.25	1.93	4.65
CMD-IONPs	9.53	6.40	3.95

[a]Targeted IONPs

[b]Non-targeted IONPs

[c]Non-treated cells with IONPs

For instance, using Table 3 and Eq. 6, the RRC_2 for BSA-IONPs is calculated as:

$$RRC_2 = \left(\frac{8.00}{68.24} \right) / \left(\frac{2.66}{68.25} \right) = 3.01.$$

In general, a value greater than one indicates that targeted IONPs are better uptaken by cells than non-targeted IONPs. Moreover, the higher RRC value for T-BSA-IONPs than T-CMD-IONPs confirms a greater cellular uptake, as seen from AAS results.

In addition, the contrast to noise ratio (CNR) between two ROIs A and B can be calculated as a ratio of the difference in grayscale averages between the two ROIs to the background noise (Bushberg and Boone 2011). Thus, the CNR is given by:

$$CNR = \frac{|SI_A - SI_B|}{\sigma_B}. \tag{7}$$

Table 4 shows the CNR values between targeted and non-targeted IONPs, as well as between them and the control group (non-treated cells with IONPS). Based on these values, the CNR between CMD-IONPs (or T-CMD-IONPs) and the control group is greater than that for BSA-IONPs (or T-BSA-IONPs). However, the CNR between targeted and non-targeted IONPs is greater than that for CMD-IONPs.

Table 3 The r_1, r_2 (mM^{-1}s^{-1}) and their ratio were measured by imaging various concentrations (C_1; 750, 500, 250, 125, 62.5 and 31.2 μM) of the synthesized IONPs in deionized water and in 1% agarose phantom gels

Contrast agent	Deionized water			In vitro			RRC[a]
	r_2	r_1	r_2/r_1	r_2	r_1	r_2/r_1	$r_2 : r_1$
BSA-IONPs	68.25	3.34	20.43	2.66	0.22	12.09	3.01:1.51
T-BSA-IONPs	68.24	3.21	21.26	8.00	0.32	25	
CMD-IONPs	159.84	14.95	10.69	5.92	0.20	29.60	2.19:1.32
T-CMD-IONPs	145.85	12.49	11.68	11.85	0.22	53.86	

[a]$RRC_{1,2} = (\frac{r_{1,2-cell}}{r_{1,2-water}})_T / (\frac{r_{1,2-cell}}{r_{1,2-water}})_{NT}$

Discussion

A great deal of progress has been made in molecular imaging techniques due to the development of peptides in recent years. The targeted radionuclide ^{68}Ga-PSMA-11, which is US Food and Drug Administration (FDA) approved, has provided a high specific PCa detection method by PET scan. Additionally, in light of the expansion of advanced MRI sequences and their role in improving PCa diagnosis sensitivity (Patel et al. 2019; Smith et al. 2019), this study sought to develop a nanomolecular MR-imaging probe by PSMA-11.

In this regard, IONPs were synthesized and coated by BSA and CMD then specified by PSMA-11-HBED and PSMA-11-HYNIC. To our knowledge, this is the first study to investigate targeted IONPs by PSMA-11 ligands.

The coating surface determines the final size of the IONPs as well as their biocompatibility. The size of the CMD-IONPs can be reduced by controlling the temperature of the reaction with a $10°C$ water bath. The BSA molecule on the other hand has a bigger size than Dextran, $69\,kDa$ versus $9-11\,kDa$, so BSA-IONPs have a bigger hydrodynamic size than CMD-IONPs. Moreover, increasing the reaction temperature results in more Fe_3O_4 than Fe_2O_3 being formed; therefore, 78 °C and 48 °C water baths were used in the preparation of CMD-IONPs and BSA-IONPs, respectively.

It should be noted that the raise in temperature for BSA-IONPs was limited because temperatures over 50 °C led to BSA protein coagulation. As a result, CMD-IONPs were deep black and BSA-IONPs were dark brown color.

Based on the aforementioned explanations, it was predictable that some Fe_2O_3 would be created in the BSA-IONPs synthesis process. Although the XRD results confirmed the formation of Fe_3O_4 in both synthesized IONPs, some Fe_2O_3 was detected in the BSA-IONPs spectrum. As a consequence, BSA-IONPS would have a lower magnetization than CMD-IONPs.

The TGA analysis affirmed that the weight of IONPs is equal to 38% of BSA-IONPs and 32% of CMD-IONPs. Accordingly, naked IONPs in BSA-IONPs and CMD-IONPs will show saturation magnetization of 95 and $156\,emu/g$, respectively.

Aside from this, IONPs are suitable for novel magnetic particle imaging (MPI). The spatial resolution of this technique is better when nanoparticles reach saturation magnetization with a smaller external magnetic field (Ghorbani et al. 2021; Knopp and Buzug 2012). Various IONPs can be compared by determining the applied field strength which causes the magnetization to reach 80% of its saturation.

This field strength for BSA-IONPs and CMD-IONPs is 2.8 and $3.0\,KOe$, respectively. Consequently, while the signal intensity of BSA-IONPs will be less than CMD-IONPs, they provide a better spatial resolution based on the physics behind MPI.

The MTT assay results signified that the toxicity of IONPs increases with concentration. Besides, corona protein is formed as a consequence of the interaction between proteins in the biological systems with the surface of IONPs (Frtús et al. 2020). These proteins face some changes which lead to the molecular mechanisms of cellular toxicity. It is thought that the higher biocompatibility of BSA-IONPs compared to CMD-IONPs has to do with the fact that hard corona of IONPs is mainly albumin based. Studies have also revealed that $10-100\,nm$ nanoparticles enter cells mainly through endocytosis, which is affected by the cell type, the physico-chemical nature of nanoparticles and the corona protein (Nagesh et al. 2016; Yu et al. 2011; Frtús et al. 2020). Smaller particles are taken up more likely via endocytosis (Frtús et al. 2020). Thus, the smaller size of CMD-IONPs can cause them to be more cytotoxic because their endocytosis is easier.

Additionally, targeted IONPs increment the cellular internalization which is confirmed by the AAS results.

As one can see from Table 2, the UR values are greater for T-BSA-IONPs than T-CMD-IONPs. This may be due to chemical functional groups on them. For more explanation, PSMA-11 is attached to PSMA by one of its carboxyl group, while PSMA-11-HBED and PSMA-11-HYNIC have six and three carboxyl groups, respectively. Therefore, T-BSA-IONPs are more likely to attach to the surface of LNCaP cells. On the other hand, samples were centrifuged at low speed and short time to remove the nanoparticles that were not completely attached to the cells. Therefore, some of the taken up nanoparticles were omitted from the environment due to toxicity and cell lysis. Although results were reported based on the number of cells counted after 24 h incubation with IONPs, they could be affected by the toxicity as explained. Furthermore, no significant difference was observed between C_1 and C_2 at $250\,\mu M$ for the URs values of the specified nanoprobes.

Moreover, the differences in UR values between C_1 and C_2 are greater for T-BSA-IONPs than T-CMD-IONPs. It could also be due to the chemical functional groups. In other words, PSMA-11-HYNIC was attached to CMD-IONPs via its only amine group, while there are more chemical functional groups available to attach PSMA-11-HBED on the BSA-IONPs.

The relaxation rates (r_1 and r_2) of IONPs and their distribution in the body affect contrast enhancement and are mainly related to their size, shape, surface coating and aggregation state (Mohammadi et al. 2020; Shevtsov et al. 2014; Maenosono et al. 2008). The r_2/r_1 ratio ≥ 10 and $r_2/r_1 \sim 5-8$ indicate a T_2 and an ideal T_1–T_2 dual-mode contrast agent, respectively (Deng et al. 2021; Zhou et al.

2014). The prepared targeted and non-targeted IONPs showed T_2 MRI contrast agent properties. A high values of r_2 and r_2/r_1 confirmed a negative contrast agent; hence, T-BSA-IONPs and T-CMD-IONPs are the most negative, respectively, in deionized water and in in vitro. Secondly, The r_2 and r_2/r_1 values are smaller in in vitro than aqueous medium. This result could be related to the number of IONPs taken up by cells.

As one can see, the r_1 values in in vitro are the same and less than one, which suggests that the IONPs stay negative contrast. Otherwise, IONPs would be a T_1–T_2 dual-mode contrast agent. Also, the same values can be a reason for some kind of spin–spin interaction, which affected the T_2 relaxation time. It is much more interesting that the relaxation rates for targeted IONPs are greater than those non-targeted in in vitro.

This is worth noticing that by increasing the external magnetic field intensity, r_1 significantly reduces, whereas r_2 slightly increases and thus r_2/r_1 sharply increases. Besides using larger nanoparticles leads to an increase of r_1 and r_2 (Deng et al. 2021). Shevtsov et al. Shevtsov et al. (2014) used super-paramagnetic iron oxide nanoparticles conjugated with epidermal growth factor for brain tumors. The r_2 and r_1 values were 247.8 and 1.4 (mM^{-1}s^{-1}) in a 7.1 T MRI scanner. Deng et al. investigated the magnetic properties of PEGylated monocrystalline super-paramagnetic iron oxide with various nanocrystal sizes and surface PEG lengths (SPIO@PEG5k) (Deng et al. 2021). Comparing CMD-IONPs with 8 nm SPIO@PEG5k, CMD-IONPs have a much larger r_2, lower r_1 and so a higher r_2/r_1 ratio (10.69 than 6.5). Hence, the mentioned SPIO@PEG5k was introduced as a T_1–T_2 dual-mode contrast agent.

Overall, T-CMD-IONPs show greater T_2 contrast agent effect, but T-BSA-IONPs offer higher targeting capabilities; hence, there is a greater RRC value for T-BSA-IONPs. This result is also consistent with the values obtained for CNR.

Conclusion

In summary, we successfully prepared appropriate, targeted, small size BSA-IONPs–PSMA-11-HBED (T-BSA-IONPs) and CMD-IONPs–PSMA11-HYNIC (T-CMD-IONPs) as specified contrast agents for prostate cancer detection. Moreover, relaxometry, cellular uptake efficiency, and cytotoxicity effects of the nanomolecular imaging probes were investigated. Briefly, our promising data suggest that super-paramagnetic T-BSA-IONPs and T-CMD-IONPs are stable, negative contrast agents and can specifically target PSMA + human prostate cancer cells.

Although T-CMD-IONPs have greater r_2 value, T-BSA-IONPs are more biocompatible and provide better cell uptake results.

Declarations

References

Abd Elrahman AA, Mansour FR (2019) Targeted magnetic iron oxide nanoparticles: preparation, functionalization and biomedical application. J Drug Deliv Sci Technol 52:702

Abdolahi M, Shahbazi-Gahrouei D, Laurent S, Sermeus C, Firozian F, Allen BJ, Boutry S, Muller RN (2013) Synthesis and in vitro evaluation of MR molecular imaging probes using J591 mAb-conjugated SPIONs for specific detection of prostate cancer. Contrast Media Mol Imaging 8(2):175

Abraham C, Jani P, Turuba R, Campbell M, Zehbe I, Curiel L (2017) In vivo 3T magnetic resonance imaging using a biologically specific contrast agent for prostate cancer: a nude mouse model. J Nanotechnology 2017:1

Afshar-Oromieh A, Babich JW, Kratochwil C, Giesel FL, Eisenhut M, Kopka K, Haberkorn U (2016) The rise of PSMA ligands for diagnosis and therapy of prostate cancer. J Nuclear Med 57(Supplement 3):79S

Ahn T, Roberts MJ, Abduljabar A, Joshi A, Perera M, Rhee H, Wood S, Vela I (2019) A review of prostate-specific membrane antigen (PSMA) positron emission tomography (PET) in renal cell carcinoma (RCC). Mol Imaging Biol 21(5):799

Basha MAA, Hamed MAG, Hussein O, El-Diasty T, Abdelkhalek YI, Hussein YO, Alasamer AF, Mohamed HA, Deen DSE, Tantawy EF et al (2019) 68Ga-PSMA-11 PET/CT in newly diagnosed prostate cancer: diagnostic sensitivity and interobserver agreement. Abdom Radiol 44(7):2545

Bates D, Abraham S, Campbell M, Zehbe I, Curiel L (2014) Development and characterization of an antibody-labeled super-paramagnetic iron oxide contrast agent targeting prostate cancer cells for magnetic resonance imaging. PLoS One 9(5):e97220

Bushberg JT, Boone JM (2011) Image quality, the essential physics of medical imaging. Philadelphia, Lippincott Williams & Wilkins, p 90

Byong Y, Kwak S (2010) Assembly of magnetite nanoparticles into spherical mesoporous aggregates with a 3-D wormhole-like porous structure. J Mater Chem 20:8320

Catalona WJ, Richie JP, Ahmann FR, Hudson MA, Scardino PT, Flanigan RC, Dekernion JB, Ratliff TL, Kavoussi LR, Dalkin BL et al (1994) Comparison of digital rectal examination and serum prostate specific antigen in the early detection of prostate cancer: results of a multicenter clinical trial of 6,630 men. J Urology 151(5):1283

Deng LH, Jiang H, Lu FL, Wang HW, Pu Y, Wu CQ, Tang HJ, Xu Y, Chen TW, Zhu J et al (2021) Size and PEG length-controlled PEGylated monocrystalline superparamagnetic iron oxide nanocomposite for MRI contrast agent. Int J Nanomed 16:201

Doustkhah E, Heydarizadeh M, Fathi Z, Mohtasham H, Rostamnia S, Hasani M (2019) Dithiocarbamate modified SPION-chitosan nanobiocomposite, a promising adsorbent for bovine serum albumin (BSA). Chem Methodol 3(5):562

Frtús A, Smolková B, Uzhytchak M, Lunova M, Jirsa M, Kubinová Š, Dejneka A, Lunov O (2020) Analyzing the mechanisms of iron oxide nanoparticles interactions with cells: a road from failure to success in clinical applications. J Controll Release 328:59

Ghorbani F, Imanparast A, Hataminia F, Sazgarnia A (2018) A novel nano-superparamagnetic agent for photodynamic and photothermal therapies: an in-vitro study. Photodiagn Photodyn Ther 23:314

Ghorbani F, Seyedi S, Montazerabadi A (2021) Magnetic particle imaging and its application. Front Biomed Technol 8(2):143

Guthman DA, Bergstralh EJ, Wilson TM, Zincke H, Blute ML, Oesterling JE (1993) Biopsy proved prostate cancer in 100 consecutive men with benign digital rectal examination and elevated serum prostate-specific antigen level: Prevalence and pathologic characteristics. Urology 42(2):150

Jalali F, Dorraji PS, Mahdiuni H (2014) Binding of the neuroleptic drug, gabapentin, to bovine serum albumin: Insights from experimental and computational studies. J Luminescence 148:347

Kiess A, Banerjee S, Mease R, Rowe S, Rao A, Foss C, Chen Y, Yang X, Cho S, Nimmagadda S et al (2015) Prostate-specific membrane antigen as a target for cancer imaging and therapy. Q J Nuclear Med Mol Imaging : Off Publ Italian Assoc Nuclear Med (AIMN) Int Assoc Radiopharmacol (IAR) Sect Soc 59(3):241

Knopp T, Buzug TM (2012) How magnetic particle imaging works, magnetic particle imaging. Springer, Berlin, pp 11–70

Li TJ, Huang CC, Ruan PW, Chuang KY, Huang KJ, Shieh DB, Yeh CS (2013) In vivo anti-cancer efficacy of magnetite nanocrystal-based system using locoregional hyperthermia combined with 5-fluorouracil chemotherapy. Biomaterials 34(32):7873

Maenosono S, Suzuki T, Saita S (2008) Superparamagnetic FePt nanoparticles as excellent MRI contrast agents. J Magn Magn Mater 320(9):L79

Mikhaylova M, Kim DK, Berry CC, Zagorodni A, Toprak M, Curtis AS, Muhammed M (2004) BSA immobilization on amine-functionalized superparamagnetic iron oxide nanoparticles. Chem Mater 16(12):2344

Mohammadi Z, Attaran N, Sazgarnia A, Shaegh SAM, Montazerabadi A (2020) Superparamagnetic cobalt ferrite nanoparticles as T_2 contrast agent in MRI: in vitro study. IET Nanobiotechnol 14(5):396

Montazerabadi AR, Oghabian MA, Irajirad R, Muhammadnejad S, Ahmadvand D, Delavari HH, Mahdavi SR (2015) Development of gold-coated magnetic nanoparticles as a potential MRI contrast agent. Nano 10(04):1550048

Nagesh PK, Johnson NR, Boya VK, Chowdhury P, Othman SF, Khalilzad-Sharghi V, Hafeez BB, Ganju A, Khan S, Behrman SW et al (2016) PSMA targeted docetaxel-loaded superparamagnetic iron oxide nanoparticles for prostate cancer. Colloids Surf B: Biointerfaces 144:8

Ngen EJ, Benham Azad B, Boinapally S, Lisok A, Brummet M, Jacob D, Pomper MG, Banerjee SR (2019) MRI assessment of prostate-specific membrane antigen (PSMA) targeting by a PSMA-targeted

magnetic nanoparticle: potential for image-guided therapy. Mol Pharm 16(5):2060

Nosrati H, Salehiabar M, Manjili HK, Danafar H, Davaran S (2018) Preparation of magnetic albumin nanoparticles via a simple and one-pot desolvation and co-precipitation method for medical and pharmaceutical applications. Int J Biological Macromol 108:909

Patel P, Wang S, Siddiqui MM (2019) The use of multiparametric magnetic resonance imaging (mpMRI) in the detection, evaluation, and surveillance of clinically significant prostate cancer (csPCa). Curr Urol Rep 20(10):1

Rahbar K, Afshar-Oromieh A, Jadvar H, Ahmadzadehfar H (2018) PSMA theranostics: current status and future directions. Mol Imaging 17:1536012118776068

Shevtsov MA, Nikolaev BP, Yakovleva LY, Marchenko YY, Dobrodumov AV, Mikhrina AL, Martynova MG, Bystrova OA, Yakovenko IV, Ischenko AM (2014) Superparamagnetic iron oxide nanoparticles conjugated with epidermal growth factor (SPION-EGF) for targeting brain tumors. Int J Nanomed 9:273

Sillerud LO (2016) Quantitative [Fe] MRI of PSMA-targeted SPIONs specifically discriminates among prostate tumor cell types based on their PSMA expression levels. Int J Nanomed 11:357

Silong H, Xiaoping X, Yao Z et al (2016) Preliminary clinical study of 99mTc-labelled small molecules against PSMA for prostate cancer imaging. China Oncol 26(7):608

Smith CP, Laucis A, Harmon S, Mena E, Lindenberg L, Choyke PL, Turkbey B (2019) Novel imaging in detection of metastatic prostate cancer. Curr Oncol Rep 21(4):1

Sun Y, Zhu Y, Huang C, Li R, Chen Y, Duan Y (2016) Magnetite loaded Polypeptide-PLGA multifunctional microbubbles for dual-mode US/MR imaging. Contrast Media Mol Imaging 11(2):146

Taylor RM, Huber DL, Monson TC, Ali AMS, Bisoffi M, Sillerud LO (2011) Multifunctional iron platinum stealth immunomicelles: targeted detection of human prostate cancer cells using both fluorescence and magnetic resonance imaging. J Nanopart Res 13(10):4717

Topală T, Bodoki A, Oprean L, Oprean R (2014) Bovine serum albumin interactions with metal complexes. Clujul Med 87(4):215

Yousefvand M, Mohammadi Z, Ghorbani F, Irajirad R, Abedi H, Seyedi S, Papi A, Montazerabadi A (2021) Investigation of specific targeting of triptorelin-conjugated dextran-coated magnetite nanoparticles as a targeted probe in GnRH+ cancer cells in MRI. Contrast Media Mol Imaging 2021:5534848

Yu MK, Kim D, Lee IH, So JS, Jeong YY, Jon S (2011) Image-guided prostate cancer therapy using aptamer-functionalized thermally cross-linked superparamagnetic iron oxide nanoparticles. Small 7(15):2241

Zhou Z, Zhao Z, Zhang H, Wang Z, Chen X, Wang R, Chen Z, Gao J (2014) Interplay between longitudinal and transverse contrasts in Fe3O4 nanoplates with (111) exposed surfaces. ACS Nano 8(8):7976